

Observation of on- and off-resonant interaction between a solid-state spin qubit and a superconducting resonator

Senlei Li¹, Shane P. Kelly², Jingcheng Zhou¹, Hanyi Lu³, Yaroslav Tserkovnyak², Hailong Wang^{1,*}, and Chunhui Rita Du^{1,3,*}

¹School of Physics, Georgia Institute of Technology, Atlanta, Georgia 30332, USA

²Department of Physics and Astronomy, University of California, Los Angeles, California 90095, USA

³Department of Physics, University of California, San Diego, La Jolla, California 92093, USA

*Corresponding authors: hwang3021@gatech.edu; cdu71@gatech.edu

Abstract: Hybrid systems consisting of multiple materials with distinct physical properties and tunable interactions provide a promising route for fulfilling transformative quantum innovations. Solid-state spin qubits and superconducting circuits stand out as leading candidates in this context due to their complementary device performance and quantum mechanical properties. Here, we report experimental integration of a single nitrogen-vacancy (NV) spin qubit and an on-chip superconducting resonator for realizing multimodal quantum applications. Specifically, we have observed superconductivity enhanced NV spin relaxation, which shows a similar Habel-Slichter peak feature around the phase transition point. In the coherent interaction regime, we show that the superconducting resonator mode is capable of exciting NV Rabi oscillations. Taking advantage of scanning NV magnetometry, we further visualized microscopic electromagnetic behaviors of the superconducting resonator, revealing the formation and evolution of superconducting vortices at the nanoscale. Our results highlight the potential of harnessing NV centers and superconducting circuits for designing hybrid systems to advance the burgeoning quantum revolution. The current study will also open a new pathway to test and evaluate miniaturized superconducting electronics for their future design and performance improvements.

Recently, hybrid systems have attracted tremendous research interest due to their advantages in harnessing distinct physical properties of individual constituents and excitations for implementing cutting-edge quantum innovations^{1,2}. A key strategy underlining these transformative sciences and technologies is to utilize intrinsic quantum mechanical properties of solid-state matter such as coherence, superposition, and strong coupling to revolutionize the performance of their conventional counterparts^{1,2}. Solid-state nitrogen-vacancy (NV) spin qubits and advanced superconducting circuits naturally stand out as two active contenders in the surge of this emerging quantum era³⁻⁷. Taking advantage of the unprecedented spatial and field sensitivity, to date, NV centers have been demonstrated as a state-of-the-art quantum sensor of microscopic electromagnetic properties in a range of “hard” and “soft” material systems⁸⁻¹⁰. On another front, revolutionary quantum computing, simulation, and network communication technologies built on superconducting circuits are rapidly growing and have achieved remarkable success over the past decade¹¹⁻¹⁴. Their highly complementary performance on quantum coherence, solid-state scalability, and electromagnetic properties establishes NV spin qubits and superconducting circuits as two attractive sub-platforms for designing hybrid devices to advance the next generation quantum technologies^{1,2}.

Despite the potential benefit and enormous promise, experimental demonstration of an integrated system consisting of a single NV center and superconducting device(s) for multimodal quantum operation remains elusive. One of the major challenges results from the vanishingly small dipole coupling strength of an isolated solid-state spin¹⁵⁻¹⁸, which imposes a tremendous technical bottleneck for building interactive quantum connections between an NV spin qubit and functional superconducting circuits at cryogenic or even lower working temperatures.

Here, we report our recent progress in this direction. Taking advantage of scanning quantum sensing techniques^{9,19-25}, we have observed on- and off-resonant dipole coupling between a single NV center^{4,8} and an on-chip niobium (Nb) superconducting resonator^{1,26-28}. We found that quasiparticle-induced magnetic noise emanating from the Nb resonator can drive spin relaxation of a proximal NV center, which shows a similar Habel-Slichter peak²⁹ feature around the superconducting transition point. In the coherent interaction regime, we show that the superconducting resonator mode is capable of exciting NV Rabi oscillations, where the driving efficiency reaches the maximum when the NV spin energy matches the resonator frequency. We further visualize the microscopic electromagnetic field responses of the Nb resonator, revealing the formation and evolution of superconducting vortices at the nanoscale. Our results highlight the potential of integrating NV spin qubits with superconducting resonators for building hybrid solid-state platform(s) for advanced technological applications^{1,2}. The presented work also demonstrates the advantages of quantum sensor(s) on evaluating local electromagnetic properties of miniaturized superconducting electronics for their future performance improvements¹¹.

Before presenting our experimental results, we first discuss the detailed device structure and measurement platform. Figure 1a shows an optical microscopy image of a lithographically defined Nb superconducting circuit consisting of a coplanar microwave feedline capacitively coupled with a resonator patterned on a sapphire substrate (see Method Section and Supplementary Information Note 1 for details). The length of the signal line is 12 mm with one-end open-circuited, resulting in a characteristic resonator frequency of ~ 2.7 GHz. We utilize an NV center contained in a diamond cantilever¹⁹ to perform quantum sensing of nanoscale electromagnetic field environment of the on-chip resonator as illustrated in Fig. 1b. An NV center consists of a substitutional nitrogen atom adjacent to a carbon atom vacancy in one of the nearest neighboring sites of a diamond crystalline lattice⁴. The negatively charged NV state has an $S = 1$ electron spin

and serves as a “three-level” quantum system^{4,8}. NV magnetometry exploits the quantum mechanical nature of the isolated spin to achieve unprecedented field and spatial sensitivity of static, microwave, and fluctuating magnetic fields under a broad range of experimental conditions^{9,10}. In the current work, our quantum sensing measurements mainly focus on the device area close to the shorted end of the signal line (Fig. 1c), where the amplitude of the microwave magnetic field generated by the resonator is expected to reach the maximum for the convenience of NV spin control. Figure 1d shows a spatially resolved microwave field distribution map obtained by performing scanning NV magnetometry measurements at 2 K over the surveyed sample region. One can see that the emanating microwave magnetic field mainly concentrates in the edges of the coplanar signal line, which is attributed to the magnetic flux expulsion effect in a superconductor³⁰. The simulated spatially dependent microwave current distribution is presented in Fig. 1e, where microwave currents flow along opposite directions in the signal and ground lines (see Supplementary Information Note 2 for details). We characterize the microwave transmission performance of the Nb resonator through the feedline using a vector network analyzer. Figure 1f presents a resonator mode spectrum measured at 2 K with zero external magnetic field. It shows a microwave absorption dip at 2.719 GHz with a full width half maximum linewidth of ~ 0.7 MHz, corresponding to a quality factor of $\sim 3,800$.

We now discuss the fluctuating dipole interaction between an NV spin qubit and the Nb resonator. For a clean superconducting system such as Nb in the current study, quasiparticles featuring elementary electron and hole excitations from broken Cooper pairs constitute one of the major sources of emanating electromagnetic noise^{29,31}. Figure 2a shows a sketch of 2D quasiparticle dispersion and occupation with a minimum energy of the *s*-wave type superconducting energy gap. Invoking the classical picture, a quasiparticle with a frequency $f + \Delta f$ can be scattered to another state with a frequency f , leading to emission of magnetic noise at a frequency Δf . When Δf matches the NV electron spin resonance (ESR) frequency f_{ESR} , quasiparticle induced magnetic noise will drive spin relaxation of a proximal NV center from $m_s = 0$ to $m_s = \pm 1$ state(s), resulting in enhanced NV relaxation rate Γ_s (Fig. 2a). We use NV spin relaxometry measurements^{19,23,32–34} (see Method Section and Supplementary Information Note 3 for details) to experimentally evaluate the electromagnetic noise generated from the superconducting resonator. Figure 2b presents the obtained temperature dependent NV spin relaxation rate Γ_s . Notably, it shows a peak value at a temperature just below the superconducting transition point T_c of Nb, which resembles the Hebel-Slichter peak observed in nuclear spin relaxation measurements of a *s*-wave superconductor²⁹. The superconductivity enhanced NV relaxation can be intuitively captured by the Bardeen–Cooper–Schrieffer (BCS) theory. In the BCS model, the magnitude of fluctuating magnetic noise depends on the density of quasiparticle states which has a square root singularity $DOS(E) \propto 1/\sqrt{E^2 - \Delta(T)^2}$, where the superconducting energy gap Δ decreases with increasing temperature and vanishes at T_c ^{29,31,35}. This singularity behavior results in the low-frequency magnetic noise probed by the NV center ($hf_{\text{ESR}} < \Delta$, h is the Planck constant) reaching a peak value around the T_c as shown in Fig. 2b³¹. When the measurement temperature is well below T_c , thermally induced electromagnetic fluctuations decrease exponentially in Nb due to the reduced quasiparticle density³¹. It is instructive to note that electromagnetic fluctuations remain active in Nb above T_c owing to free electron-induced Johnson-Nyquist noise in the conventional normal metal phase³². The observed superconducting phase transition dependent NV relaxation is in agreement with a generic theoretical model that we have developed, corroborating the physical picture discussed above (see Supplementary Information Note 4 for details)³¹. In addition to temperature, external microwave magnetic fields serve as

another tuning knob to control quasiparticle excitations in superconductors. When the Nb resonator is driven to the resonant state, quasiparticle density will dramatically increase due to collective photon absorption as shown in Fig. 2c³⁶. This will naturally lead to a stronger noncoherent NV-resonator dipole interaction owing to larger fluctuating magnetic fields produced by quasiparticles. Figure 2d presents the NV relaxation rate Γ_s measured as a function of the external microwave driving frequency f . One can see that Γ_s reaches a maximum when f matches the resonator frequency f_R . Under the resonant condition ($f = f_R$), Γ_s exhibits a characteristic polynomial increasing behavior as a function of the input microwave power P due to the nonlinear photon-quasiparticle interaction³⁶.

Next, we present optically detected magnetic resonance (ODMR) and Rabi measurement results (See Methods Section for details)^{19,33}, providing alternative perspectives to examine the dipole interaction between the NV spin qubit and superconducting resonator. The NV center was scanned to a lateral position above the coplanar signal line in these measurements as shown in Fig. 3a. Note that the Oersted microwave field produced by the distant feedline decays over the space showing a negligible value at the NV site. In this case, the inductive microwave magnetic field B_R generated by the signal line plays a dominant role in controlling the NV spin state. We first performed ODMR measurements to investigate the on- and off-resonant coupling between the NV center and the superconducting resonator. Figure 3b shows the normalized NV photoluminescence intensity as a function of the applied microwave frequency f and external magnetic field B_{ext} recorded at 6 K. Interestingly, we observed two curved lines of f_+ and f_- emerging at ~ 2.88 GHz, which is due to the decrease of NV fluorescence when the microwave drive frequency f matches the NV ESR conditions⁸. Here, f_+ and f_- represent the ESR frequencies corresponding to NV spin transitions between the $m_s = 0$ and $m_s = \pm 1$ states, respectively. Deviation from the conventional straight ESR lines is attributed to the Meissner effect of superconducting Nb³⁰, which partially shields the effective magnetic field experienced by the NV center. Notably, NV photoluminescence is also reduced when f matches the resonator frequency f_R . The off-resonant coupling effect becomes significantly pronounced when f_R approaches and matches the NV ESR frequency as highlighted by a zoomed-in view shown in Fig. 3c. Figure 3d plots a linecut at $B_{\text{ext}} = 45$ G of the presented NV ODMR map measured over a broad range of microwave power. One can see that the resonator mode and NV ESR features emerge at the corresponding frequencies. The demonstrated ODMR detection of the resonator mode confirms the off-resonant dipole interaction between a single NV spin qubit and a proximal on-chip superconducting resonator, which is absent when the measurement temperature is above the T_c of Nb (see Supplementary Information Note 5 for details).

We now extend discussion of the on-resonant dipole interaction showing superconducting resonator mode driven collective NV Rabi oscillations. NV Rabi cycle refers to periodical oscillations between two quantum spin states in the Bloch sphere as illustrated in Fig. 3e³⁷. It can be experimentally achieved by applying a microwave magnetic field at the NV ESR frequencies, and the induced spin rotation rate f_{Rabi} is proportional to the amplitude of the local driving magnetic field transverse to NV spin axis (Fig. 3e)^{8,37}. Here, we utilize a measurement protocol shown on the top panel of Fig. 3f to optically detect NV Rabi oscillations by measuring spin-dependent NV photoluminescence (see Methods Section and Supplementary Information Note 6 for details). The bottom panel of Fig. 3f presents three representative Rabi spectra measured at 6 K. When f_- is detuned from the resonator frequency f_R by 61 MHz, the NV photoluminescence spectrum slowly oscillates at a Rabi frequency f_{Rabi} of 2.6 MHz. When the detuning frequency decreases to 26 MHz, we observe clearly accelerated oscillation behavior of the NV

photoluminescence spectrum with an enhanced f_{Rabi} of 10.1 MHz. f_{Rabi} further increases to a peak value of ~ 20.1 MHz when the NV spin energy matches the frequency of the resonator mode. The significant increase of f_{Rabi} results from a larger microwave magnetic field (B_{R}) generated by the superconducting resonator mode. Figure 3g plots f_{Rabi} measured as a function of the external magnetic field B_{ext} . It is evident that the presented coherent NV spin control becomes the most efficient at the experimental condition of $f_{-} = f_{\text{R}}$.

The dual nature of an NV center being a spin qubit and a sensor highlights its potential for both quantum computing and quantum metrology research and technological applications³. Lastly, we ascertain this unique advantage by performing NV imaging of nanoscale electromagnetic field response, specifically the formation of superconducting vortices, of the on-chip Nb resonator (See Supplementary Information Note 7 for details). In an intuitive physical picture, vortices could be viewed as individual magnetic flux quanta generated from circulating supercurrents around a conducting core as illustrated in Fig. 4a. Vortices in a superconductor can be locally controlled by defects, thermal heating, electric current flow, external magnetic fields, and other kinds of external stimuli^{21,22,38}. Here, we utilize scanning NV magnetometry to visualize magnetic flux induced superconducting vortices in the on-chip Nb resonator. A magnetic field B_z perpendicular to the sample surface was introduced to generate superconducting vortices in Nb during the field cooling process. B_z was kept in the follow-up scanning NV measurements. The magnitude of the net magnetic field at the NV site is obtained from the split NV spin energy, which can be optically detected by ESR measurements (See Supplementary Information Note 7 for details)^{21,22,38}. Figure 4b shows a magnetic field map of a surveyed device area of the Nb signal line with $B_z = 1.7$ G at 2 K. Circularly shaped vortices visually stand out by exhibiting significantly pronounced local penetrating magnetic fields in comparison with surrounding superconducting sample areas where magnetic flux is partially shielded by the Meissner screening effect²¹. The magnetic flux generated by individual vortices is estimated to be $22.2 \text{ G } \mu\text{m}^2$ (see Supplementary Information Note 7 for details), in qualitative agreement with the theoretical prediction²¹ of one flux quantum $h/2e$. When B_z increases to 2.7 G, the density of formed superconducting vortices enhances, and their lateral dimensions decrease accordingly due to the conservation of magnetic flux penetrating through the superconducting Nb as shown in Fig. 4c. Figure 4d shows a zoomed-in view of a single vortex formed in the Nb signal line. We further performed scanning NV Rabi measurements to investigate the spatially dependent microwave magnetic field response of a vortex. A separate external microwave field (B_{mw}) is introduced to the on-chip Nb resonator by an integrated Au wire attached to the diamond cantilever and here we aim to image how a superconducting vortex modifies its proximal microwave field environment. Similar to the situation of static penetrating magnetic field(s), B_{mw} shows larger values when the NV center is positioned right above the superconducting vortex due to the AC Meissner effect, leading to faster NV Rabi oscillation frequencies as shown in Figs. 4e-4f. Considering the dissipating nature, vortices formed in superconducting circuits can introduce malignant electromagnetic noise to induce quantum decoherence of proximal qubits as well as random perturbations on qubit operations³⁹. We share the optimism that the cutting-edge quantum sensing approaches presented in the current work will pave the way for future design, test, and evaluation of energy dissipation, functionalities, and microwave tunability of a broad range of superconducting circuits.

In summary, we have demonstrated quantum sensing of microscopic electromagnetic behaviors in an on-chip superconducting resonator. We show that local microwave magnetic fields generated by the resonator mode can coherently control an NV spin qubit, whose driving efficiency reaches a maximum when the resonator frequency matches NV ESR conditions. We also observed

quasiparticle mediated fluctuating dipole interaction between an NV spin and the resonator via both NV relaxometry and ODMR measurements. The measured NV spin relaxation rate shows a peak value around the T_c of Nb, revealing a similar Hebel-Slichter peak²⁹ feature in *s*-wave superconductors. A detailed knowledge of the microscopic electromagnetic noise profile of superconducting resonators will provide insights on future qubit design to reduce quantum decoherence for qubit readout and entanglement operations⁴⁰. Spatially dependent magnetic field response of the Nb resonator is further imaged by scanning NV magnetometry, visualizing the formation and evolution of superconducting vortices on a length scale of tens of nanometers. Our results highlight the potential of NV centers and superconducting circuits for building hybrid systems for state-of-the-art quantum innovations. The cryogenic scanning quantum metrology techniques will also provide a new, previously unexplored way to evaluate nanoscale electromagnetic properties of solid-state superconducting devices, advancing their applications for designing next-generation quantum electronics^{1,2,41}.

Acknowledgements. The authors are grateful to Zelong Xiong and Mengqi Huang for valuable help on device preparations and characterizations. This work was primarily supported by the Office of Naval Research (ONR) under grant No. N00014-23-1-2146. Development of the scanning NV microscopy was supported by the U.S. Department of Energy (DOE), Office of Science, Basic Energy Sciences (BES), under award No. DE-SC0024870. H. L. was supported by the Air Force Office of Scientific Research (AFOSR) under award No. FA9550-21-1-0125. C. R. D. also acknowledged the support from Alfred. P. Sloan Foundation (FG-2024-21387). The work at UCLA was supported by U.S. National Science Foundation (NSF) under grant No. DMR-2049979.

References

1. Xiang, Z.-L., Ashhab, S., You, J. Q. & Nori, F. Hybrid quantum circuits: Superconducting circuits interacting with other quantum systems. *Rev. Mod. Phys.* **85**, 623–653 (2013).
2. Clerk, A. A., Lehnert, K. W., Bertet, P., Petta, J. R. & Nakamura, Y. Hybrid quantum systems with circuit quantum electrodynamics. *Nat. Phys.* **16**, 257–267 (2020).
3. Awschalom, D. D., Bassett, L. C., Dzurak, A. S., Hu, E. L. & Petta, J. R. Quantum spintronics: engineering and manipulating atom-like spins in semiconductors. *Science* **339**, 1174–1179 (2013).
4. Doherty, M. W. *et al.* The nitrogen-vacancy colour centre in diamond. *Phys. Rep.* **528**, 1–45 (2013).
5. Childress, L. & Hanson, R. Diamond NV centers for quantum computing and quantum networks. *MRS Bull.* **38**, 134–138 (2013).
6. Awschalom, D. D., Hanson, R., Wrachtrup, J. & Zhou, B. B. Quantum technologies with optically interfaced solid-state spins. *Nat. Photon.* **12**, 516–527 (2018).
7. de Leon, N. P. *et al.* Materials challenges and opportunities for quantum computing hardware. *Science* **372**, eabb2823 (2021).
8. Rondin, L. *et al.* Magnetometry with nitrogen-vacancy defects in diamond. *Rep. Prog. Phys.* **77**, 056503 (2014).
9. Casola, F., van der Sar, T. & Yacoby, A. Probing condensed matter physics with magnetometry based on nitrogen-vacancy centres in diamond. *Nat. Rev. Mater.* **3**, 17088 (2018).
10. Aslam, N. *et al.* Quantum sensors for biomedical applications. *Nat. Rev. Phys.* **5**, 157–169 (2023).
11. Devoret, M. H. & Schoelkopf, R. J. Superconducting circuits for quantum information: an outlook. *Science* **339**, 1169–1174 (2013).
12. Arute, F. *et al.* Quantum supremacy using a programmable superconducting processor. *Nature* **574**, 505–510 (2019).
13. Zhang, X., Kim, E., Mark, D. K., Choi, S. & Painter, O. A superconducting quantum simulator based on a photonic-bandgap metamaterial. *Science* **379**, 278–283 (2023).
14. Magnard, P. *et al.* Microwave quantum link between superconducting circuits housed in spatially separated cryogenic systems. *Phys. Rev. Lett.* **125**, 260502 (2020).
15. Dolde, F. *et al.* Room-temperature entanglement between single defect spins in diamond. *Nat. Phys.* **9**, 139–143 (2013).
16. Kubo, Y. *et al.* Strong coupling of a spin ensemble to a superconducting resonator. *Phys. Rev. Lett.* **105**, 140502 (2010).
17. Zhu, X. *et al.* Coherent coupling of a superconducting flux qubit to an electron spin ensemble in diamond. *Nature* **478**, 221–224 (2011).
18. Hu, Y., Song, Y. & Duan, L. Quantum interface between a transmon qubit and spins of nitrogen-vacancy centers. *Phys. Rev. A* **96**, 062301 (2017).
19. Li, S. *et al.* Observation of stacking engineered magnetic phase transitions within moiré supercells of twisted van der Waals magnets. *Nat. Commun.* **15**, 5712 (2024).
20. Song, T. *et al.* Direct visualization of magnetic domains and moiré magnetism in twisted 2D magnets. *Science* **374**, 1140–1144 (2021).
21. Thiel, L. *et al.* Quantitative nanoscale vortex imaging using a cryogenic quantum magnetometer. *Nat. Nanotechnol.* **11**, 677–681 (2016).
22. Pelliccione, M. *et al.* Scanned probe imaging of nanoscale magnetism at cryogenic temperatures with a single-spin quantum sensor. *Nat. Nanotechnol.* **11**, 700–705 (2016).

23. Finco, A. *et al.* Imaging non-collinear antiferromagnetic textures via single spin relaxometry. *Nat. Commun.* **12**, 767 (2021).
24. Monge, R. *et al.* Spin dynamics of a solid-state qubit in proximity to a superconductor. *Nano. Lett.* **23**, 422–428 (2023).
25. Palm, M. L. *et al.* Observation of current whirlpools in graphene at room temperature. *Science* **384**, 465–469 (2024).
26. Hou, J. T. & Liu, L. Strong coupling between microwave photons and nanomagnet magnons. *Phys. Rev. Lett.* **123**, 107702 (2019).
27. Xu, Q. *et al.* Strong photon-magnon coupling using a lithographically defined organic ferrimagnet. *Adv. Sci.* **11**, 2310032 (2024).
28. Li, Y. *et al.* Strong coupling between magnons and microwave photons in on-chip ferromagnet-superconductor thin-film devices. *Phys. Rev. Lett.* **123**, 107701 (2019).
29. Hebel, L. C. & Slichter, C. P. Nuclear Spin relaxation in normal and superconducting aluminum. *Phys. Rev.* **113**, 1504–1519 (1959).
30. Wang, X., Laav, M., Volotsenko, I., Frydman, A. & Kalisky, B. Visualizing current in superconducting networks. *Phys. Rev. Appl.* **17**, 024073 (2022).
31. Kelly, S. P. & Tserkovnyak, Y. Superconductivity-enhanced magnetic field noise. Preprint at <https://doi.org/10.48550/arXiv.2412.05465> (2024).
32. Kolkowitz, S. *et al.* Probing Johnson noise and ballistic transport in normal metals with a single-spin qubit. *Science* **347**, 1129–1132 (2015).
33. McCullian, B. A. *et al.* Broadband multi-magnon relaxometry using a quantum spin sensor for high frequency ferromagnetic dynamics sensing. *Nat. Commun.* **11**, 5229 (2020).
34. Zu, C. *et al.* Emergent hydrodynamics in a strongly interacting dipolar spin ensemble. *Nature* **597**, 45–50 (2021).
35. Zarea, M., Ueki, H. & Sauls, J. A. Effects of anisotropy and disorder on the superconducting properties of niobium. *Front. Phys.* **11**, 4 (2023).
36. Goldie, D. J. & Withington, S. Non-equilibrium superconductivity in quantum-sensing superconducting resonators. *Supercond. Sci. Technol.* **26**, 015004 (2012).
37. Fuchs, G. D., Dobrovitski, V. V., Toyli, D. M., Heremans, F. J. & Awschalom, D. D. Gigahertz dynamics of a strongly driven single quantum spin. *Science* **326**, 1520–1522 (2009).
38. Lillie, S. E. *et al.* Laser modulation of superconductivity in a cryogenic wide-field nitrogen-vacancy microscope. *Nano. Lett.* **20**, 1855–1861 (2020).
39. Song, C. *et al.* Microwave response of vortices in superconducting thin films of Re and Al. *Phys. Rev. B* **79**, 174512 (2009).
40. Wang, C. *et al.* Measurement and control of quasiparticle dynamics in a superconducting qubit. *Nat. Commun.* **5**, 5836 (2014).
41. Chatterjee, S. *et al.* Single-spin qubit magnetic spectroscopy of two-dimensional superconductivity. *Phys. Rev. Res.* **4**, L012001 (2022).

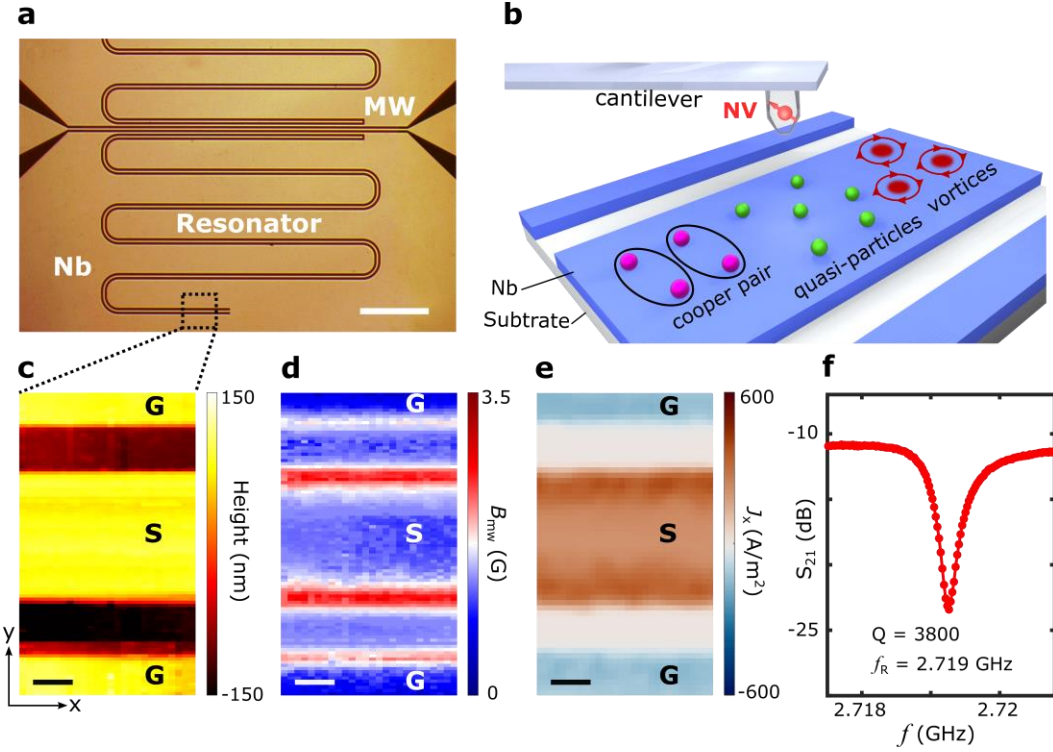


Figure 1. Scanning quantum sensing of an on-chip superconducting resonator. **a** Optical image of a patterned Nb resonator device. Scale bar is $500 \mu\text{m}$. **b** Schematic illustration of scanning NV sensing of quasiparticles and superconducting vortices in the coplanar signal line of the on-chip Nb resonator. **c** AFM imaging of the topography of a surveyed device area of the Nb coplanar waveguide, which is close to the shorted end of the signal line. **d** Scanning NV imaging of spatially dependent microwave magnetic field B_{mw} distribution in the surveyed device area. The vertical NV-to-sample distance is ~ 500 nm, input microwave power is 20 dBm, and measurement temperature is 2 K. **e** Simulated microwave current J_x distribution in the Nb resonator. Scale bar in **c-e** is $6 \mu\text{m}$. **f** Microwave transmission of the superconducting resonator mode measured at 2 K without external magnetic field.

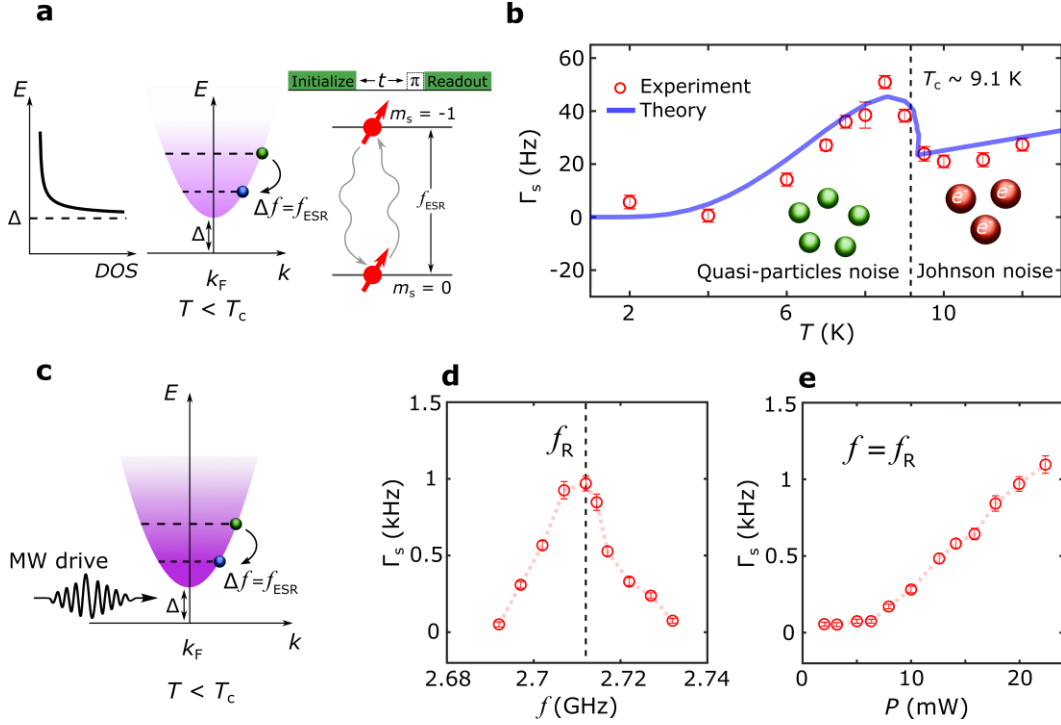


Figure 2. Detecting quasiparticle-induced magnetic noise by an NV center. **a** Sketch of 2D dispersion and density of states (DOS) of quasiparticles in a s -wave superconductor. The occupation function follows the Fermi-Dirac distribution as indicated by the fading colors. “Two-quasiparticle” scattering induced magnetic noise at ESR frequencies drives spin relaxation of a proximal NV center. Top right: pulsed optical and microwave sequences for NV spin relaxometry measurements. **b** NV spin relaxation rate Γ_s measured as a function of temperature between 2 K and 12 K. Γ_s is driven by fluctuating magnetic fields generated by quasiparticles or Johnson–Nyquist noise from electrons below and above the T_c of Nb, respectively. **c** Microwave excitation at the resonator frequency increases the quasiparticle density in Nb and the emanating magnetic noise. **d** NV spin relaxation rate Γ_s shows a peak value when the frequency f of external driving microwave field matches the frequency f_R of the Nb resonator mode. The input external microwave power is 20 mW (13 dBm). **e** Γ_s measured as a function of microwave power under the resonant condition ($f = f_R$). The measurement temperature is 6 K, and the NV-to-sample distance is ~ 100 nm for results presented in Figs. 3b, 3d, and 3e. Γ_s is recorded at $f_{\text{ESR}} = 2.865$ GHz for presented NV spin relaxometry results.

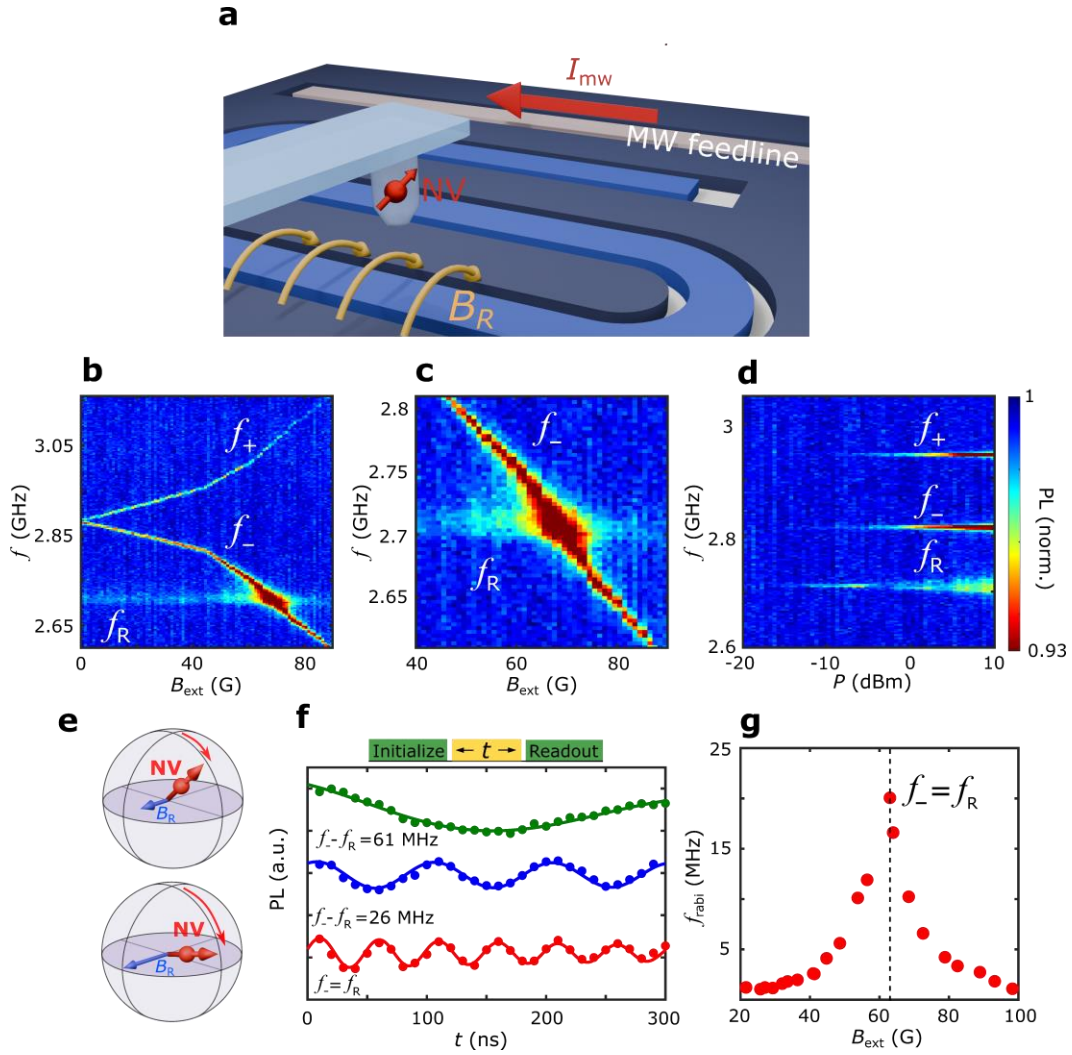


Figure 3. On- and off-resonant dipole interaction between a single NV spin qubit and a superconducting resonator. **a** Schematic of local NV spin control by the inductive microwave magnetic field B_R generated by the signal line of an on-chip Nb resonator. **b** ODMR map shows normalized NV photoluminescence (PL) as a function of external magnetic field B_{ext} applied along the NV spin direction and microwave frequency f . **c** Zoomed-in view of the ODMR map when the resonator frequency f_R approaches and crosses f_- . **d** A linecut at $B_{\text{ext}} = 45$ G of the ODMR map measured over a broad range of input microwave power from -20 dBm to 10 dBm. **e** Schematic of NV Rabi oscillations on the Bloch sphere. A larger transverse microwave magnetic field B_R will drive a faster spin rotation rate. **f** Top panel: pulsed microwave and optical sequences for NV Rabi oscillation measurements. Bottom panel: NV Rabi spectra recorded at the detuning frequency ($f_- - f_R$) of 61 MHz, 26 MHz, and 0 MHz. **g** NV Rabi frequency measured as a function of the external magnetic field B_{ext} . The dashed lines highlight the condition where f_- matches f_R . The NV-to-sample distance is fixed at ~ 500 nm and measured temperature is 6 K for presented NV ODMR and Rabi results.

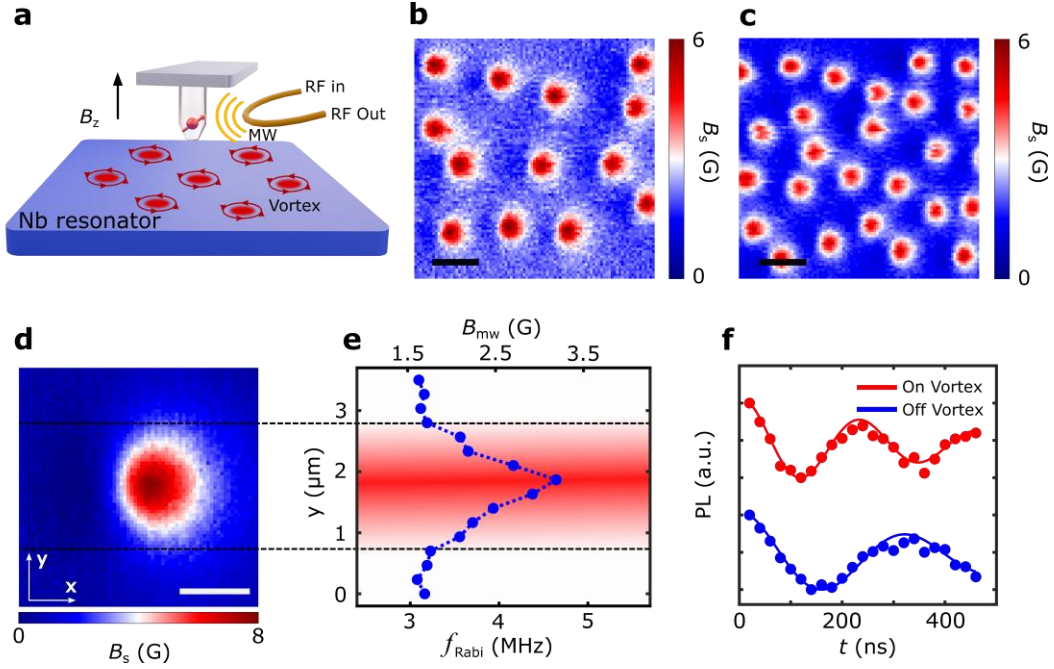


Figure 4. Nanoscale imaging of superconducting vortices in an on-chip Nb resonator. **a** Visualizing superconducting vortices using a scanning NV spin sensor with an integrated microwave antenna. **b-c** Static magnetic field (B_s) maps of vortices formed in the Nb resonator with a perpendicular magnetic cooling field B_z of 1.7 G (**b**) and 2.7 G (**c**). Scale bar is 2 μm and measurement temperature is 2 K. **d** Zoomed-in view of a single superconducting vortex formed in Nb. Scale bar is 1 μm . **e** One-dimensional spatial dependence of measured Rabi frequency when scanning the NV center over the superconducting vortex. The NV spin shows enhanced Rabi frequencies when being positioned within the physical defines (highlighted by the shaded red color) of the vortex due to AC Meissner effect. **f** Two representative Rabi spectra recorded when the NV center stands right above and away from the superconducting vortex. The vertical NV-to-sample distance is fixed at 100 nm for presented scanning NV imaging results.